Check for updates

Advanced Functional Materials

ADVANCED FUNCTIONAL MATERIALS
www.afm-journal.de

ARTICLE OPEN ACCESS

Exploring Curvature Effects in Direct-Written 3D Curved Hollow Magnetic Nanoshells

Oleksii M. Volkov[1,2] | Fabrizio Porrati[2] | Florian Kronast[3] | Riccardo Hertel[4] | Pavlo Makushko[1] | Olha Bezsmertna[1] | Alexander Kuprava[2] | Mohamad-Assaad Mawass[3,5] | Sven Barth[2] | Michael Huth[2] | Denys Makarov[1]

[1]Helmholtz-Zentrum Dresden-Rossendorf e.V., Institute of Ion Beam Physics and Materials Research, Dresden, Germany | [2]Physikalisches Institut, Goethe-Universität Frankfurt am Main, Frankfurt am Main, Germany | [3]Helmholtz-Zentrum Berlin für Materialien und Energie, Berlin, Germany | [4]CNRS, Institut de Physique et Chimie des Matériaux de Strasbourg, Université de Strasbourg, Strasbourg, France | [5]Department of Mathematics and Physics, American University of Ras Al Khaimah, Ras Al Khaimah, UAE

Correspondence: Oleksii M. Volkov (volkov@physik.uni-frankfurt.de)

Received: 1 September 2025 | **Revised:** 30 April 2026 | **Accepted:** 19 May 2026

Keywords: curvature-induced effects | curved hollow magnetic nanoshells | domain wall | focused electron beam-induced deposition

ABSTRACT

Recent advances in additive nanofabrication have enabled the realization of free-standing three-dimensional architectures with precisely controlled geometry and material composition at the nanoscale. Here, we investigate the magnetic properties of 3D PtC/Co_3Fe core–shell heterostructures with engineered curvature and shell thickness profiles. Using focused electron-beam-induced deposition in combination with temperature-induced site-selective chemical vapor deposition, we realize hollow magnetic nanoshells with different cross-section, curvature and thickness profiles with outer dimensions down to 200 nm. Using X-ray magnetic circular dichroism photoelectron emission microscopy (XMCD-PEEM) and full-scale micromagnetic simulations, we reveal distinct curvature- and thickness-dependent magnetization reversal mechanisms with the formation of axially symmetric Néel domain walls (DWs) separating vortex domains with opposite circulations. We quantify the role of uncompensated magnetostatic charges in curved hollow geometries and show how curvature and thickness asymmetry shape the micromagnetic energy landscape, DW pinning and the corresponding stray-field distributions.

1 | Introduction

Geometric features start playing an increasingly prominent role in condensed matter physics, as they allow going beyond standard material properties determined by the intrinsic composition through changes of geometrical parameters [1, 2]. The latter are especially relevant in the case of low-dimensional systems, where curvature, symmetry and topology introduce novel physical effects by modifying electronic [2], plasmonic [3] and magnetic responses at the nanoscale [1, 4]. In particular, in magnetism, the interplay between the three-dimensional (3D) vector nature of the order parameter and geometry gives rise to a rich spectrum of emergent phenomena, including geometrically-induced chiral interactions [5–7], topological spin textures [8–10] and magnetization configurations with high-order vorticity [11]. These effects create opportunities to design functional materials with controlled magnetic responses without the need for extensive material screening approaches.

Recent advances in additive nanomanufacturing techniques, such as two-photon lithography [12–15], charged aerosol jet nanoprinting [16] and focused electron-beam-induced deposition (FEBID) [17–20], have significantly improved the fabrication of 3D nanostructures with nanoscale precision and design

This is an open access article under the terms of the Creative Commons Attribution License, which permits use, distribution and reproduction in any medium, provided the original work is properly cited.
© 2026 The Author(s). *Advanced Functional Materials* published by Wiley-VCH GmbH

flexibility. Unlike conventional lithography [21, 22], these direct-write techniques enable the fabrication of free-standing 3D architectures with complex designs [3, 20, 23–25], which introduce geometrically-driven effects in solid-state physics in a controlled and scalable manner. In magnetism, FEBID-written structures enable the experimental verification of geometrically-induced effects [11, 26, 27] and offer convenient integration of curvilinear objects into standard spintronic architectures [28], while preserving high spatial resolution. Still, the direct FEBID fabrication of hollow and tubular magnetic nanostructures, which are of considerable theoretical and practical interest, due to their striking magnetochiral properties of dipolar origin [29–31] and ultrafast domain wall (DW) motion [32–34], encounters fundamental limitations due to the proximity and electron scattering effects [35–37]. The latter are caused by unintended precursor dissociation beyond the beam focus and corresponding filling of the hollow part during the writing process, which compromises the quality and controllability of the fabricated nanostructures. To overcome these limitations, hybrid fabrication methods have recently been developed that combine FEBID for precise formation of 3D non-magnetic scaffolds followed by conformal electrochemical magnetic deposition [38] or heat-induced in situ chemical vapor deposition (CVD) of FEBID precursors [39]. In the latter case, the utilization of Joule heating of a FEBID scaffold under controlled precursor atmosphere enables spatially localized shell growth and formation of high-purity (up to 85 atom%) crystalline thin shells [39, 40]. These methods ensure both structural reproducibility and functionalized coating critical for 3D superconductive and spintronic applications relying on geometrical and curvilinear effects [1].

Here, we report the fabrication and detailed magnetic investigation of self-standing 3D PtC/Co_3Fe core–shell heterostructures with engineered curvature and shell thickness profiles. In contradistinction to typically studied straight hollow magnetic nanotubes with circular [32, 33, 41–48] and hexagonal [49–51] cross-sections, we utilize FEBID in combination with a site-selective CVD process to realize hollow magnetic nanoshells (generalized cylindrical shells) with controlled principal curvatures within a single material platform, see Figure 1. Specifically, we engineer two distinct types of shells: one exhibiting a relatively homogeneous first principal curvature distribution, κ_1, and a strongly inhomogeneous second principal curvature, κ_2, and a second type with a geometric constriction that yields strongly inhomogeneous κ_1 and κ_2. Using advanced X-ray magnetic circular dichroism photoelectron emission microscopy (XMCD-PEEM) and comprehensive micromagnetic simulations, we reveal distinct reversal mechanisms governed by geometric curvature and cross-sectional thickness asymmetry of Co_3Fe shell and identify the formation of axially symmetric Néel-type vortex-homogeneous-vortex domain walls (DWs) separating vortex domains with opposite circulations [49, 52]. In addition, numerically simulated direct and shadow XMCD-PEEM contrasts, calculated for micromagnetically obtained states, qualitatively reproduce the main features of the experimentally observed contrasts. Moreover, both the XMCD-PEEM measurements and the simulations consistently reveal curvature-induced pinning of DWs at specific regions along the nanoshell. By evaluating the associated stray-field and vector-potential distributions, we quantify the role of uncompensated magnetostatic charges in curved hollow geometries and show how curvature and thickness asymmetry shape the micromagnetic energy landscape and DW pinning.

2 | Results and Discussions

2.1 | Magnetic Nanoshells With Inhomogeneous Second Principal Curvature

3D core–shell nanostructures are fabricated by means of a two-step hybrid approach [39]: (i) the fabrication of a carbon rich Pt 3D stripe scaffold by means of FEBID and subsequent secondary electron irradiation, see Figure 1a; (ii) formation of a hollow Co_3Fe magnetic nanoshell around the PtC core by means of heat-induced site-selective CVD process, see Figure 1b. The first step represents the direct-write fabrication of self-standing 3D scaffold architectures at the nanoscale by using electron beam induced dissociation of the $(CH_3)_3CH_3C_5H_4Pt$ precursor gas into a PtC structure [35], see Figure 1a. As a result of the FEBID process, two PtC bridges with the widths $w_1 = 170$ nm and $w_2 = 470$ nm, respectively, are formed by moving the electron beam between two Cr/Au contacts, which enables precise control over the shape and dimensions of the scaffolds. After completion of the FEBID process, an additional electron beam irradiation is carried out without any precursor to reduce the porosity of the structure and improve its conductivity [53], see Figure 1a. This is important for the second fabrication step, when a DC current is applied to the PtC scaffold and the site-selective CVD process starts in the atmosphere of $HFeCo_3(CO)_{12}$ precursor gas without any direct electron beam irradiation [39]. Subsequently, a conformal Co_3Fe magnetic shell is formed around the PtC core due to the precursor thermal decomposition by means of Joule heating above the critical temperature of 423 K [39], see Figure 1b. The 3D scaffold geometry naturally introduces thermal gradients from the large Cr/Au contacts that act as a room temperature heat bath, toward the hottest elevated PtC part, which results in the formation of a Co_3Fe shell tapering toward the Cr/Au contacts. However, as shown previously in Ref. [39], the resulting nanoshell is mainly uniform in thickness along its length and only exhibits longitudinal thinning near the Cr/Au contacts due to heat dissipation effects. Thus, in the following analysis we will consider curved hollow nanoshells as uniform in thickness. It should also be noted that thermal decomposition of the $HFeCo_3(CO)_{12}$ precursor gas is independent of the substrate, while the interphase solid-state diffusion is negligible due to low temperatures and short growth time [39]. Still, small variations in the local conductivity of the PtC scaffold may promote surface roughness due to the formation of Co_3Fe crystallites, although this process can be controlled by adjusting the current amplitude and growth time.

After the fabrication, the resulting core–shell PtC/Co_3Fe heterostructures are morphologically characterized using scanning electron microscopy (SEM) that confirms the formation of two different flattened 3D structures with almost the same length of about $L = 4.8$ μm, but different total widths of $W_1 = 200$ nm and $W_2 = 500$ nm, see Figure 1d,f respectively. Thus, the average thickness of the Co_3Fe shells is estimated to be $H = (W_{1,2} - w_{1,2})/2 = 15$ nm, still the thickness distribution in the cross-section depends on the dimensions of the PtC scaffold and its relative position with respect to the gas injection system (GIS)

16163028, 2026, 50, Downloaded from https://advanced.onlinelibrary.wiley.com/doi/10.1002/adfm.202523172 by Helmholtz-Zentrum Berlin Für, Wiley Online Library on [20/07/2026]. See the Terms and Conditions (https://onlinelibrary.wiley.com/terms-and-conditions) on Wiley Online Library for rules of use; OA articles are governed by the applicable Creative Commons License

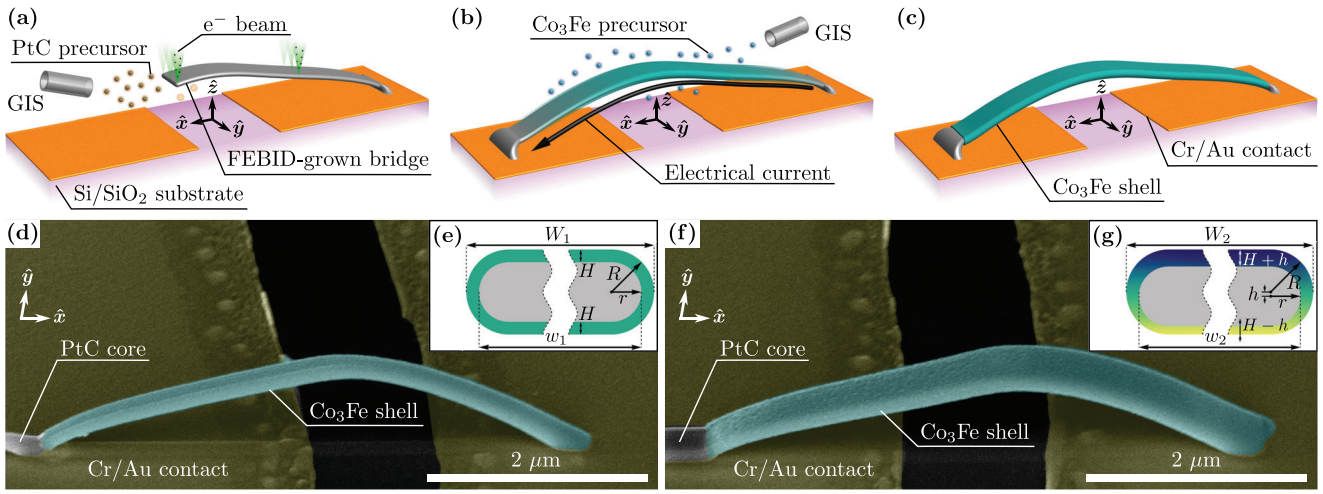

FIGURE 1 | Experimental realization of PtC/Co_3Fe core–shell curved heterostructures. (a–c) Schematics of the two-step fabrication process of a core–shell heterostructures: (a) Fabrication of a 3D PtC nanostructure by means of FEBID with its subsequent electron beam (green cone) postgrowth irradiation; (b) Formation of Co_3Fe shell by means of site-selective CVD induced by Joule heating from DC current applied though the 3D PtC scaffold (black arrow). (c) The resulting curved core–shell heterostructure with a hollow ferromagnetic shell formed around the PtC core. (d,f) and (e,g) Artificially colored scanning electron microscopy images and cross-sections schematics of narrow and wide PtC/Co_3Fe heterostructures, respectively. Different SEM parts are highlighted by color for visual clarity: light-blue for Co_3Fe shell region and yellow for Cr/Au flat contacts. The cross-sectional schematics show two different Co_3Fe shell thickness distributions with symmetric and asymmetric profiles [39].

upon the CVD process, see Figure 1e,g. In particular, in the case of wide PtC scaffolds the concentration of the $HFeCo_3(CO)_{12}$ precursor gas above the scaffold is higher than below it, so the resulting magnetic shell on the top surface grows faster than on the bottom during the thermal decomposition [39]. In the case of wide core–shell heterostructures, the introduced thickness asymmetry, $\eta = H^{top}/H^{bot}$, can reach the ratio $\eta \approx 2$ [39], while in the case of narrow heterostructures such asymmetry in thickness distribution tends to $\eta \approx 1$. In the following analysis, we assume that the thickness distribution of the magnetic shell in the case of narrow heterostructures is symmetrical and equal to $H_1 = \langle H \rangle =$ 15 nm everywhere in the cross-section, see Figure 1e. In the case of a wide 3D geometries, the existing thickness asymmetry is modeled by shifting the centre of the Co_3Fe shell toward the top side of the PtC core by $h = 5$ nm, such that the local thicknesses are $H_2^{top} = H + h = 20$ nm and $H_2^{bot} = H - h = 10$ nm, that are consistent with $\eta \approx 2$.

Each fabricated 3D heterostructure is elevated by approximately 800 nm above the substrate and exhibits spatially curved geometry with a maximum first principal curvature of $\kappa_1^{MAX} = 0.5\ \mu m^{-1}$ at the apex, see Figure 1 and Section S1. Due to their longitudinal elongation and modest apex curvatures, the resulting spatial distribution of κ_1 along the arc length, s, is rather homogeneous, with only small gradients peaking at midpoints. In contrast, the conformal Co_3Fe coating of the flattened PtC core introduces a strongly inhomogeneous second principal curvature, κ_2, with its maximum $\kappa_2^{MAX} = 1/R = 20\ \mu m^{-1}$ at the out layer with $R =$ 50 nm, see Section S1. While the fabricated core–shell heterostructures lack geometrical constrictions, the resulting spatial distribution of κ_2 depends solely on the position across the cross-section being independent of arc length s.

To investigate the magnetic behavior of the curved hollow magnetic nanoshells, hysteresis-like measurements are performed by means of XMCD-PEEM at the L_3 absorption edge of Co, see Section S2. As both 3D core–shell heterostructures have a curved, elongated, flattened and elevated shape, their gradual slope variation allows for XMCD-PEEM imaging in two modes: (i) *direct imaging* of the top surface of the bridge and (ii) *shadow imaging* of the entire geometry [54, 55], see Figure 2a,b. In the first mode, the X-ray beam directly illuminates the top surface of the hollow magnetic shell, emitting photoelectrons from the top ≈10 nm layer, the yield of which depends on beam polarization (circular clockwise and counter-clockwise) and relative magnetization distribution with respect to the incident direction. The resulting spatially resolved XMCD contrast is determined by the normalized difference between two photoelectron yield intensity measurements recorded for both polarizations and reveals magnetization vectors that are parallel (red), antiparallel (blue), and perpendicular (white) with respect to the direction of the incident X-ray beam, see Figure 2b. The second approach is used to image 3D magnetic structures, whereby a passing X-ray beam carries integral magnetic information along its path inside the 3D structure due to the depth- and helicity-dependent absorption. The transmitted part of which generates photoelectron yield from the shadow case on the substrate being sensitive to the bulk magnetization distribution [54–56], see Figure 2b. To generate the observed shadow, which resembles all features of the 3D geometry, the X-ray beam falls at the incident angle of 16° to the substrate surface and 32° azimuth angle with respect to the longitudinal direction of the tubular geometries. Thus, the resulting shadow also contains information about geometric features and the magnetization distribution inside the sample. It is important to note that due to the 3D hollow shell magnetic geometry, the shadow XMCD contrast cannot be simply interpreted as a magnetization projection along the beam direction, unlike to the direct contrast. Still, as a rule of thumb, blue/red shadow contrasts generally indicate parallel/antiparallel

16163028, 2026, 50, Downloaded from https://advanced.onlinelibrary.wiley.com/doi/10.1002/adfm.202523172 by Helmholtz-Zentrum Berlin Für, Wiley Online Library on [20/07/2026]. See the Terms and Conditions (https://onlinelibrary.wiley.com/terms-and-conditions) on Wiley Online Library for rules of use; OA articles are governed by the applicable Creative Commons License

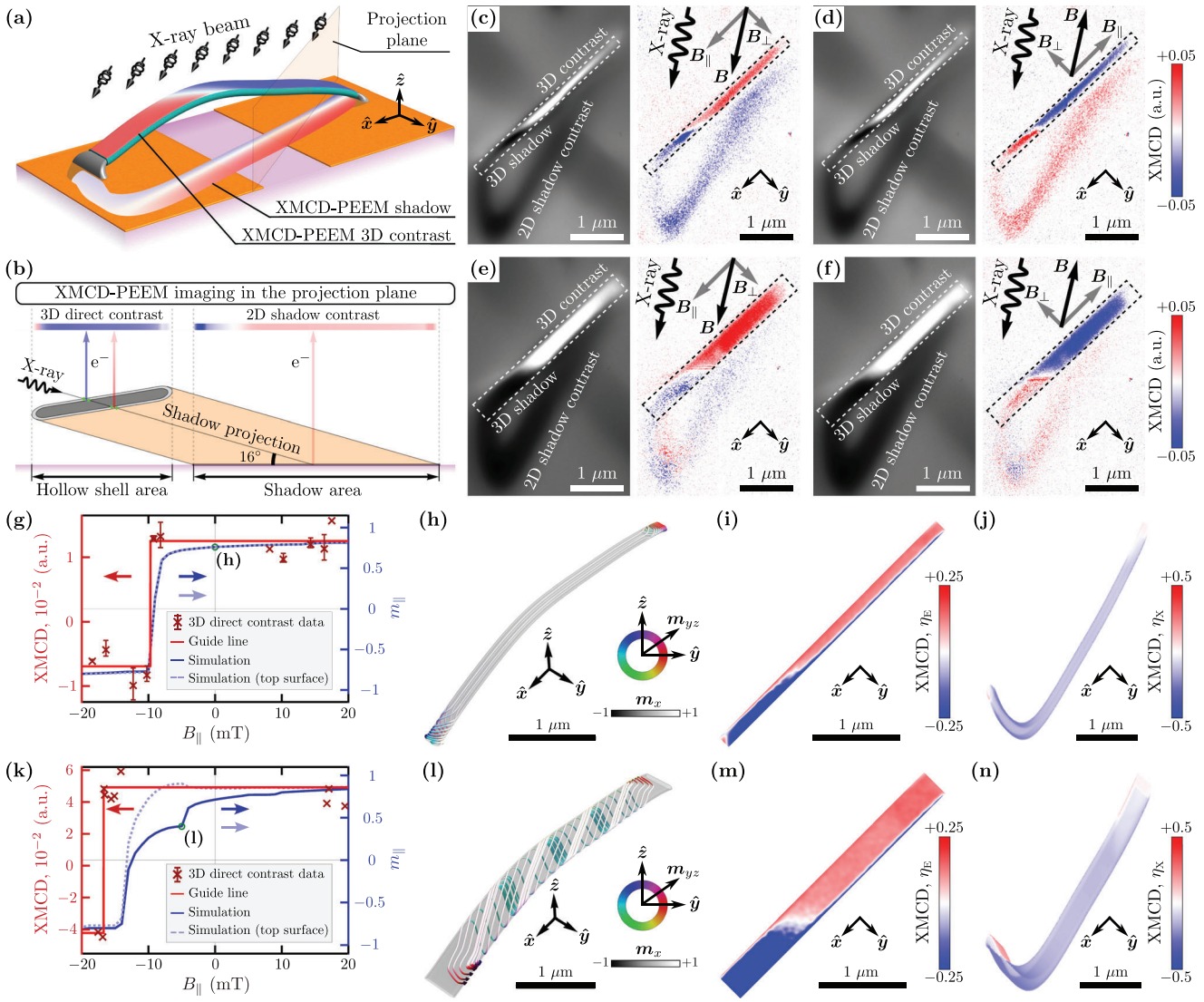

FIGURE 2 | Magnetic investigation of curved hollow magnetic nanoshells. (a) 3D schematics of XMCD-PEEM imaging of a PtC/Co_3Fe core–shell nanostructure fabricated by combined FEBID and site-selective CVD methods. The X-ray beams, shown by the black helical arrows, illuminate the 3D curved core–shell structure at an acute angle of 16°. (b) 2D schematics showing the formation of direct 3D and shadow 2D XMCD contrasts in the projection plane of the incident X-ray beams are indicated in the panel (a). (c,d) and (e,f) PEEM images and the corresponding XMCD-PEEM contrasts of the narrow and wide PtC/Co_3Fe heterostructures imaged mapped under different magnetic field orientations, parallel and antiparallel with respect to the X-ray beam, respectively. Black wavy arrows represent the direction of the incident X-ray beam, while black straight arrows show the direction for the applied external magnetic field, $\boldsymbol{B}$, with $\boldsymbol{B}_{\parallel}$ and $\boldsymbol{B}_{\perp}$ corresponding to the longitudinal and transverse field components, respectively. (g) and (k) Comparison of hysteresis-type measurements of the experimentally obtained averaged 3D direct XMCD contrast signal (red crosses) and normalized magnetization, $m_{||}$, along the $B_{\parallel}$ obtained from full-scale simulations (blue line) for both types of hollow shells. The red line shows the fit to the experimental data and the light blue dashed line shows the recalculated hysteresis signal obtained only from the top surface of the simulated 3D hollow shell magnetic geometry. (h) and (l) Equilibrium in-field magnetic states obtained from micromagnetic hysteresis simulations for the narrow ($B_{\parallel} = 0$ mT) and wide ($B_{\parallel} = -5$ mT) curved hollow magnetic nanoshells, respectively. (i,j) and (m,n) Simulated both 3D direct and 2D shadow XMCD contrasts for both types of hollow magnetic shells.

magnetization alignments due to the helicity-dependent absorption and the corresponding contrast inversion in the transmitted X-ray beam [55], see Figure 2b.

Magnetic imaging of the fabricated core–shell heterostructures is performed at remanence after applying an external in-plane magnetic field directed along the X-ray beam direction. The magnetic hollow shell geometries are imaged stepwise during a hysteresis switching between $B_{max} = +50$ mT and $B_{min} = -50$ mT in the direct imaging mode, where the XMCD-PEEM signals are collected from the top surfaces of the nanoshells, see Figure 2c–f. The latter results in the appearance of a direct contrast from the illuminated part of the 3D geometry and a corresponding inverted contrast from the 3D shadow part, see Figure 2c–f. The obtained hystereses for the narrow and wide core–shell heterostructures reveal the presence of only one distinct switching event at −9 mT and −17 mT, respectively (Figure 2g,k), which separates two states with predominantly uniform red and blue 3D direct and

16163028, 2026, 50, Downloaded from https://advanced.onlinelibrary.wiley.com/doi/10.1002/adfm.202523172 by Helmholtz-Zentrum Berlin Für, Wiley Online Library on [20/07/2026]. See the Terms and Conditions (https://onlinelibrary.wiley.com/terms-and-conditions) on Wiley Online Library for rules of use; OA articles are governed by the applicable Creative Commons License

3D shadow XMCD contrasts, see Figure 2c–f. It should be noted that both direct and shadow contrasts of the heterostructures show gradual color transitions toward the ends, indicating a magnetization reorientation from tangential distributions in the middle of heterostructures to tilted azimuthal vortex-like configurations. In the case of the narrow magnetic hollow shell, all XMCD contrasts obtained from the 3D part and the 2D shadow are homogeneous for both magnetic configurations shown in Figure 2c,d, which indicate the simultaneous switching of the top and bottom surfaces during the reversal process. In the case of the wide hollow shell, uniform XMCD contrasts are only observed in the 3D direct and 3D shadow signals, while the 2D shadow contrasts exhibit a characteristic red-white-blue pattern. The latter indicates the presence of regions with different magnetization orientations at the top and bottom surfaces of the hollow shell.

To understand the switching processes for both types of hollow magnetic nanoshells and to explain their different shadow contrasts, full-scale micromagnetic simulations are performed using the experimentally determined magnetic geometries with different shell thickness profiles. In the case of the narrow magnetic nanoshell with symmetric thickness distribution, the hysteresis simulation completely reproduces the experimentally observed magnetic switching at −9 mT, which validates the introduced micromagnetic model. The detailed reversal analysis reveals the switching between two equilibrium tangentially magnetized states with vortex-like distributions of opposite circulation localized at each end of the curved hollow nanoshell, see Figure 2h. Such a mixed magnetic configuration minimizes magnetostatic energy by forming a closed-flux state at the ends, while maintaining a quasi-uniform magnetization distribution along the nanoshell [42, 57]. The corresponding simulated 3D direct XMCD contrast (Figure 2i) shows uniform red/blue contrasts for illuminated/shadow parts of the top surface of the hollow magnetic nanoshell, while the 2D shadow XMCD contrast exhibits inverted uniformly colored blue contrast, see Figure 2j, which correctly reproduce the experimentally obtained contrasts. During the switching process, the vortex-like structures expand from the ends toward the centre through the formation of extended vortex domains with opposite circulation, while the quasi-uniform state decreases in size to a narrow tangentially magnetized region. This configuration results in the formation of an axially symmetric Néel DW, which represents a topologically stable transition region between the two vortex domains of opposite circulation [49, 52], see Section S3 for more details. Such a vortex-homogeneous-vortex (VHV) DW is the inverted counterpart of the conventional vortex DW (VDW) obtained in magnetic nanowires [58, 59] and nanotubes [44, 59]. Whereas VDW features a central vortex separating axial domains, the axial Néel or VHV DW is formed between azimuthal domains, as observed experimentally in hexagonal nanotubes [49] and electrodeposited curved ones [38]. Notably, the VHV DWs are also directly imaged by XMCD-PEEM at curvilinear defects in the additionally fabricated curved core–shell heterostructures, see Section S4.

In contrast to the one-step hysteresis loop of the narrow hollow nanoshell, the wide magnetic shell with the asymmetrical thickness distribution exhibits a three-step reversal process featuring two distinct switching events, see Figure 2k. Although the reversal process also starts from a quasi-uniform magnetization distribution with vortex-like boundary states, their circulations are identical and extend over larger areas near the ends at the bottom surface due to the thickness asymmetry of the Co_3Fe shell. The first switching event at $B_{\parallel}^{1} = -5$ mT corresponds to the reversal of the thinner bottom section of the hollow nanoshell, which reflects the transition from the mixed state to a tilted transverse distribution along the bottom surface, see Figure 2l and Section S3. This transformation is attributed to the lower switching field of the thinner region, which arises from its reduced local shape anisotropy and consequently smaller coercivity. The corresponding simulated direct and shadow XMCD contrasts exhibit the formation of red direct and blue shadow contrasts of the 3D top surface, which resemble the experimentally obtained contrasts, see Figure 2e,m. In addition, the 2D shadow contrast reveals a characteristic red-white-blue pattern, which is consistent with the experimentally obtained contrast configuration, see Figure 2e,n.

The second switching event at $B_{\parallel}^{2} = -14$ mT corresponds to the reversal of the thicker top part of the nanoshell. The latter is accompanied by the formation and extension of two diagonal 90° DWs between three homogeneously magnetized regions: two along the field and one parallel to the initial magnetization direction, see Section S3 for more details. As the external magnetic field increases, the central tangentially magnetized domain shrinks and disappears. This occurs with the formation of two vortex–antivortex pairs near the apex of the curved magnetic hollow nanoshell, which eventually annihilate, finalizing the transition to the switched mixed magnetic state, see Section S3. It should be noted that the difference between the two-step experimentally obtained and three-step numerically determined hystereses arises from the surface-sensitive nature of the direct XMCD-PEEM imaging. Namely, the electron yield from the bottom layer of the shell is significantly attenuated by the thicker top layers of the PtC core and the top Co_3Fe layer, which makes the reversal of the bottom surface undetectable in direct contrast. To demonstrate this surface sensitivity, additional numerical calculations of the hysteresis loop solely for the top surface are performed for the wide hollow magnetic nanoshell, see Figure 2k. These calculations reproduce the two-step reversal observed experimentally and resemble the measured XMCD-PEEM data, see Figure 2k. However, the existing discrepancy between the numerically and experimentally determined switching fields may indicate the presence of additional pinning. The latter could be associated with the higher roughness of the wide core–shell heterostructure originating from the higher DC currents used in the site-selective CVD process (see Methods) and corresponding local variations in micromagnetic properties. These factors increase the effective coercivity compared to the smooth micromagnetic model and indicate the role of nanoscale defects in the magnetization reversal dynamics of core–shell heterostructures.

2.2 | Micromagnetic Simulations of Geometry-Induced Effects

Since XMCD-PEEM experiments of additionally fabricated curved core–shell heterostructures reveal pinned VHV DWs stabilized at curvilinear defects (see Section S4), it becomes crucial to understand the interplay between curvature-induced effects

16163028, 2026, 50, Downloaded from https://advanced.onlinelibrary.wiley.com/doi/10.1002/adfm.202523172 by Helmholtz-Zentrum Berlin Für, Wiley Online Library on [20/07/2026]. See the Terms and Conditions (https://onlinelibrary.wiley.com/terms-and-conditions) on Wiley Online Library for rules of use; OA articles are governed by the applicable Creative Commons License

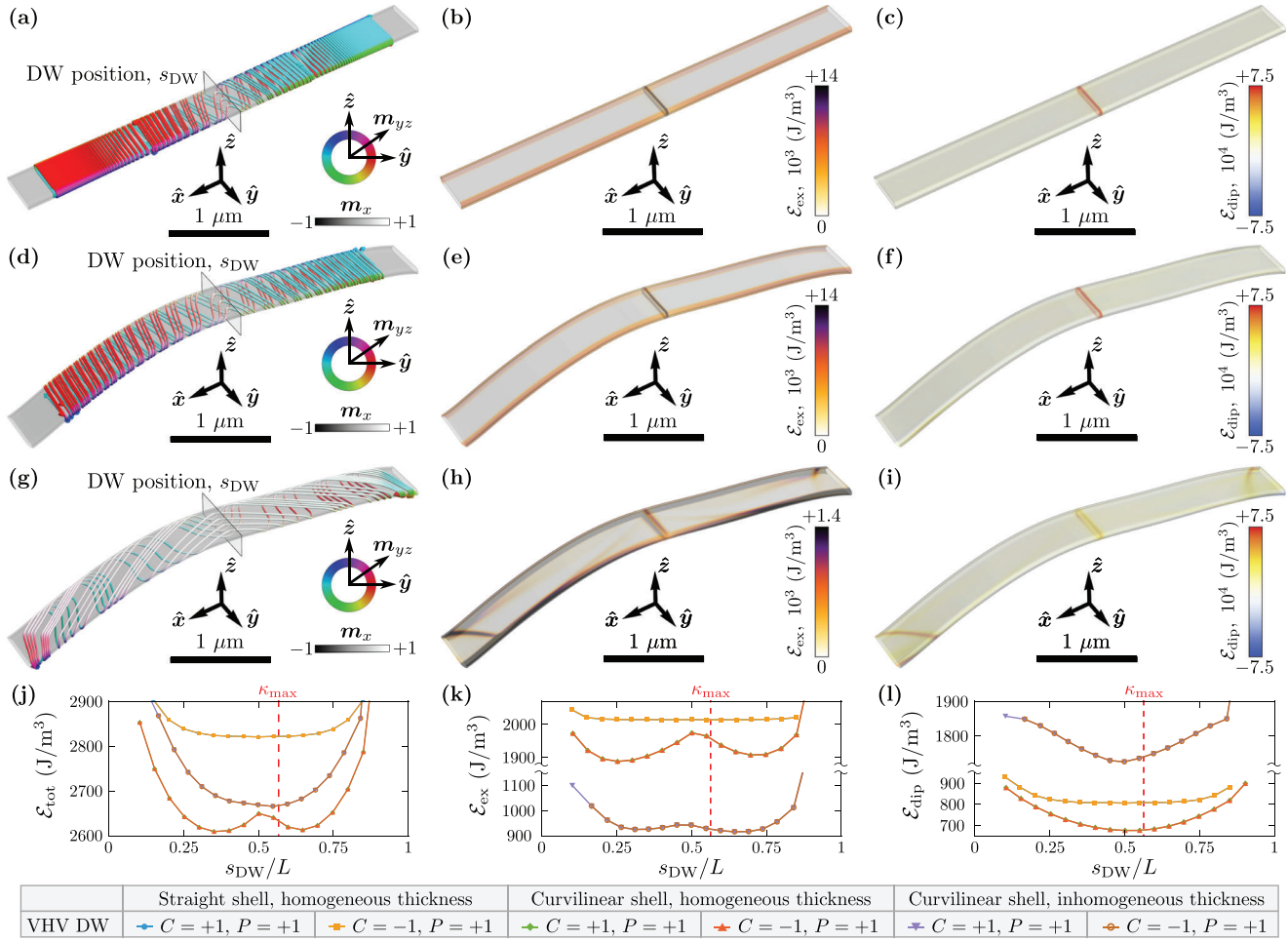

FIGURE 3 | Micromagnetic analysis of VHV DW structures and energetic landscapes in hollow magnetic nanoshells. (a), (d) and (g) Spatial magnetization distributions of the VHV DW in straight and curved wide hollow magnetic nanoshells with different cross-section profiles. Colored stream lines indicate the local magnetization directions within the Co_3Fe shells. (b), (e) and (h) Local spatial distributions of exchange energy density, $\mathcal{E}_{ex}$, in different hollow shells. (d), (f) and (i) Spatial configurations of magnetostatic energy density, $\mathcal{E}_{dip}$, for the VHV DWs in straight and curved wide hollow magnetic nanoshells with different cross-section profiles. (j) Average total micromagnetic energy density, $\mathcal{E}_{tot}$, as a function of the normalized VHV DW position s_{DW} along the hollow nanoshell, with L being its total arc length. Simulations are performed for VHV DWs with different circulation, $C = \pm 1$, and the same polarity, $P = +1$. (k) and (l) Average exchange and magnetostatic energy densities for different VHV DW positions along straight and curved wide hollow magnetic nanoshells with different cross-section profiles.

and thickness asymmetries in hollow magnetic nanoshells. To investigate this interplay, we perform additional micromagnetic simulations of the straight and curvilinear models of the wide curved hollow magnetic nanoshell with the same arc length and different shell thickness profiles. VHV DWs with various circulation, $C = \pm 1$, and polarity, $P = +1$, are introduced into the system through pre-defined states positioned at different locations along the hollow magnetic nanoshell, after which they relax to their equilibrium distributions, see Section S5. This approach enables a systematic comparison of the morphology and corresponding energy landscapes of stabilized VHV DWs under varying geometric and thickness conditions.

In the case of the straight hollow magnetic nanoshell with homogeneous thickness distribution, the uniform magnetic shell stabilizes clearly distinguishable vortex domains of opposite circulation separated by a narrow wall with longitudinal magnetization, see Figure 3a. This VHV DW configuration emerges from the simultaneous minimization of exchange and magnetostatic energy densities, which is enabled by the high geometric symmetry (axial and mirror) and toroidal topology. Specifically, the upper and lower shell parts being flat, symmetric and in close proximity obtain mutual magnetostatic coupling that favours antiparallel alignment between them, while the toroidal topology naturally introduces vortex domain formation at the ends to satisfy flux-closure constraint. Consequently, the exchange energy density distribution exhibits a local increase around the VHV DW due to the sharp magnetization rotation between counter-circulating vortex domains and at the sides of the nanoshell due to the non-zero second principal curvature ($\kappa_2 \neq 0$), see Figure 3b. Simultaneously, magnetostatic energy density distribution reveals a local increase in the VHV DW, followed by a decrease to near-zero values in vortex domains due to the corresponding flux-closure in their magnetization distributions, see Figure 3c. The micromagnetic simulations performed for different positions of VHV DWs along the nanoshell reveal the formation of energy plateaus in distributions of the total, $\mathcal{E}_{tot}(s_{DW})$, exchange, $\mathcal{E}_{ex}(s_{DW})$, and magnetostatic, $\mathcal{E}_{dip}(s_{DW})$,

16163028, 2026, 50, Downloaded from https://advanced.onlinelibrary.wiley.com/doi/10.1002/adfm.202523172 by Helmholtz-Zentrum Berlin Für, Wiley Online Library on [20/07/2026]. See the Terms and Conditions (https://onlinelibrary.wiley.com/terms-and-conditions) on Wiley Online Library for rules of use; OA articles are governed by the applicable Creative Commons License

average energy densities as a function of the DW position, s_{DW}, along the arc length of the shell, see Figure 3j–l. These flat energy landscapes with only slight elevations near the ends indicate the high mobility of VHV DWs in straight hollow nanoshells with the homogeneous thickness distribution and provide important reference values for the understanding of curvature-induced effects.

In the case of the curved hollow magnetic nanoshell with the homogeneous thickness distribution, the uniform magnetic shell also stabilizes a VHV DW between vortex domains of opposite circulation, see Figure 3d and Section S5. Similarly to the case of straight hollow shell, the exchange and magnetostatic energy distributions exhibit only a local increase around the VHV DW due to magnetization rotation, see Figure 3e,f. However, micromagnetic simulations of differently positioned VHV DWs along the curvilinear nanoshell reveal the formation of two distinct localized energy minima in the total average energy density $\mathcal{E}_{tot}(s_{DW})$, which corresponds to the formation of two pinning sites in sloped regions with $\kappa_1' \simeq 0$, see Figure 3j and Figure S2. A component-resolved analysis of $\mathcal{E}_{ex}(s_{DW})$ and $\mathcal{E}_{dip}(s_{DW})$ demonstrates that these minima originate primarily from local exchange energy reductions in low-curvature shell segments (Figure 3k), while the magnetostatic average energy density shows a broad central minimum due to minimized effects of the shell ends, see Figure 3l. Such negative curvature-driven pinning correlates with the experimentally observed stabilization of VHV DWs in curvilinear nanoshells with curvilinear defects, see Section S4. The resulting energy landscape of the VHV DW with well-defined potential minima in straight regions is reminiscent of VDW pinning recently observed in curved nanotubes [59]. This similarity highlights a dominant role of local curvilinear effects of exchange origin and also suggests the presence of negative curvature-induced driving of both types of DWs to areas with the smallest curvature. This behavior of VHV DW and VDW is in stark contrast to the pinning mechanism of a transversal DW (TDW) in nanowires [59, 60] and nanostripes [5], where TDW tends to pin at local curvature maxima due to the positive curvature-induced driving [61].

In the case of the curved magnetic hollow shells with inhomogeneous thickness profile, the asymmetry between top and bottom parts of the nanoshell introduces imbalance of their magnetostatic charges and corresponding shape-induced anisotropies. The latter leads to the formation of different magnetic domains in the upper and lower parts of the shell, which are separated by the resulting DW magnetization configuration being inherently 3D and asymmetric, see Figure 3g. Namely, the narrow bottom part of the nanoshell exhibits the formation of the VHV DW separating two vortex-like transverse domains, that transforms into tilted domains separated by the DW on the top part, see Figure 3g. Moreover, due to the disparity in tilt angles of the magnetic domains at the top and bottom surfaces, additional tilted DWs emerge near the ends of the nanoshell, which additionally complicates the local magnetic configuration. These tilted DWs represent transitional regions that accommodate the mismatch between magnetization orientations induced by the thickness gradients and curvature effects.

The presence of such complex 3D domain structures influences local distributions of both exchange and magnetostatic energy densities, that exhibit spatial variation at the ends and sides of the wide hollow nanoshell with asymmetric thickness profile, see Figure 3h,i. Specifically, two distinct VHV DW components at the top and bottom parts of the nanoshell enhance the magnetization misalignment, which leads to an increased energy cost of maintaining a non-uniform magnetic configuration in comparison to a magnetic nanoshell with homogeneous thickness profile.

Simultaneously, the magnetostatic energy density becomes strongly inhomogeneous on the top and bottom surfaces, due to the emergence of additional volume magnetostatic charges, see Figure 3i. These charges arise, in particular, near the thickness gradient and curved regions, amplifying stray fields that contribute to localized magnetostatic energy maxima. Together, the exchange and magnetostatic contributions reshape the total micromagnetic energy landscape for VHV DWs stabilized at different locations along the hollow magnetic nanoshell. Namely, the coordinate dependence of the total energy reveals the formation of a distinct single energy minimum near the apex of the nanoshell with $\kappa_{max} = 0.5\ \mu m^{-1}$, see Figure 3j. The component-wise analysis shows the presence of two minima in the exchange energy profile along the coordinate (Figure 3k), reflecting favourable DW positions at slope regions with reduced κ_1 curvature, while the magnetostatic energy exhibits a single energy minimum at the middle of the shell, due to the balance of volume and surface magnetostatic charges for the VHV DW at such position, see Figure 3l. Despite similar coordinate dependencies of VHV DW energies in curved hollow nanoshells with symmetric and asymmetric thickness profiles, steeper magnetostatic energy gradients in the asymmetric case introduces significant influence on the equilibrium position of the DW.

These results demonstrate that local geometric features, such as principal curvatures and shell thickness gradients, serve as effective measures for engineering local energetic landscapes to control DW stability and dynamics in core–shell 3D geometries. The utilization of these effects allows for the deterministic design of pinning sites and complex domain structures in 3D magnetic hollow shells, which has direct implications for future spintronic devices. Moreover, it should be noted that such curved magnetic nanoshells with inhomogeneous thickness profile could also host non-local magnetic effects originating from the interplay between curvature, symmetry and magnetostatic interactions [31]. Namely, to manifest non-local magnetic effects, it is essential to have asymmetrical magnetic geometry and magnetization texture that features both in-plane and out-of-plane magnetic components exhibiting different parity [31]. These non-local effects offer an additional layer of control over magnetic textures, potentially enabling the stabilization of chiral states, as it was demonstrated in the case of chiral deformation of vortex strings in asymmetrical Permalloy nanocaps [6].

2.3 | Simulated Stray-Field and Vector Potential LandScapes of 3D Curved Hollow Magnetic Nanoshells

The complex texture of VHV DWs in curved hollow magnetic nanoshells generates a highly localized magnetic stray field around the DW core. While vortex domains provide effective

16163028, 2026, 50, Downloaded from https://advanced.onlinelibrary.wiley.com/doi/10.1002/adfm.202523172 by Helmholtz-Zentrum Berlin Für, Wiley Online Library on [20/07/2026]. See the Terms and Conditions (https://onlinelibrary.wiley.com/terms-and-conditions) on Wiley Online Library for rules of use; OA articles are governed by the applicable Creative Commons License

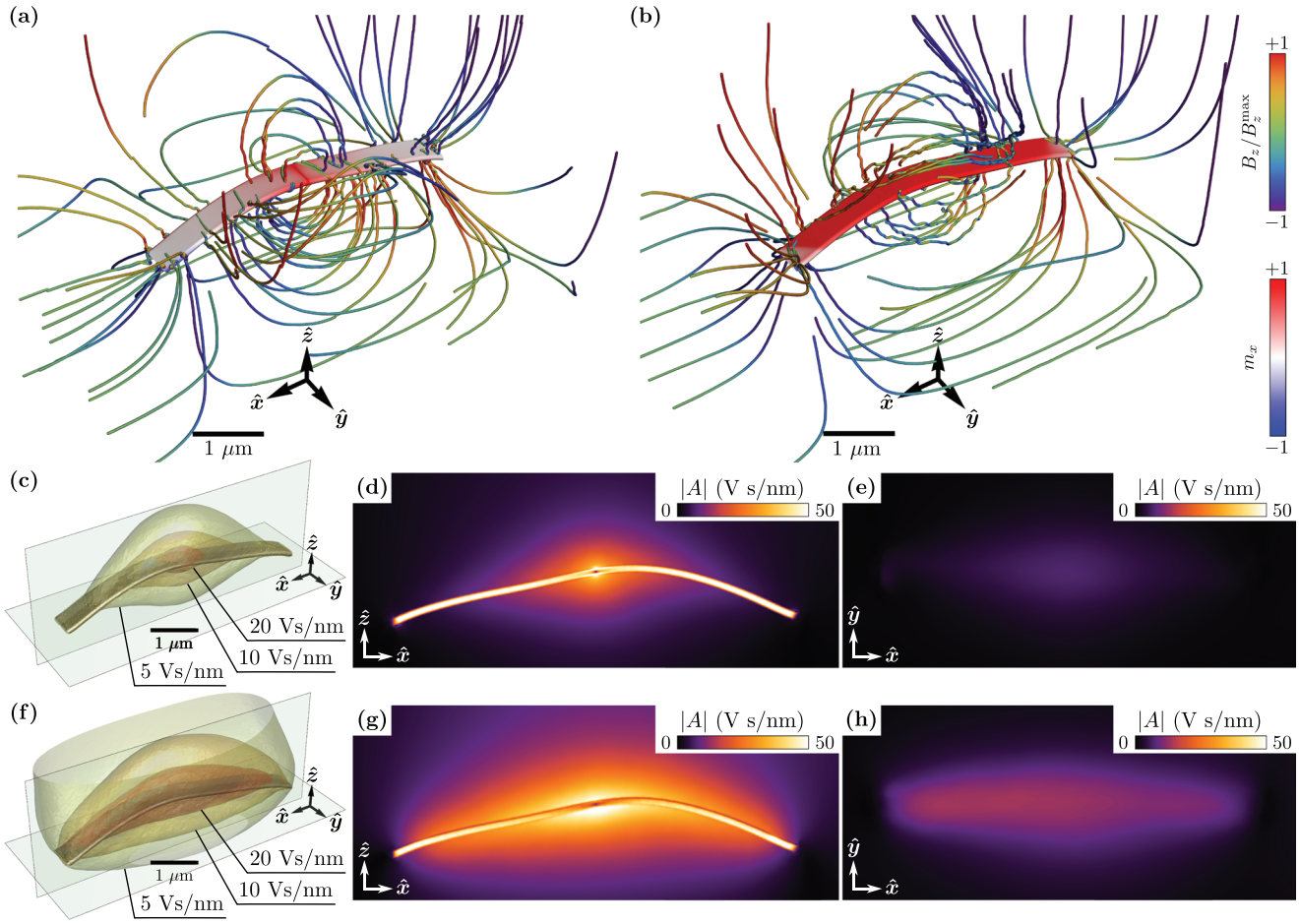

FIGURE 4 | Stray fields and vector potentials around curved hollow magnetic nanoshells. (a) and (b) Stray magnetic field lines that have been obtained for the stabilized VHV DW in hollow magnetic nanoshells with homogeneous and inhomogeneous thickness profiles. The red-white-blue contrast shows the distribution of the m_x component along the shell, while the rainbow contrast represents the normalized B_z component of the stray field $\boldsymbol{B}$. (c) and (f) 3D distributions of vector potential magnitudes, $|\boldsymbol{A}|$, around the stabilized VHV DW in both types of magnetic shells with the indicated $\hat{\boldsymbol{x}}\hat{\boldsymbol{z}}$ and $\hat{\boldsymbol{x}}\hat{\boldsymbol{y}}$ planes going through and below the flattened magnetic tube shells. (d,e) and (g,h) Spatial distributions of vector potential magnitudes across $\hat{\boldsymbol{x}}\hat{\boldsymbol{z}}$ and $\hat{\boldsymbol{x}}\hat{\boldsymbol{y}}$ planes for hollow magnetic nanoshells with homogeneous and inhomogeneous thickness profiles. The color indicates the strength of the vector potential magnitude.

magnetic flux closure, the central longitudinal part retains uncompensated charges that produce tight field loops and pronounced near field variations, see Figure 4a,b. To quantify these stray field distributions, we perform additional numerical calculations of the vector field potential, $\boldsymbol{A}$, using the Ampère approach on the equilibrium magnetic configurations, see Figure 4. In both cases of curved hollow magnetic nanoshells with symmetric and asymmetric thickness profiles, VHV DWs generate complex closed field loops around the VHV DWs, see Figure 4a,b. Despite the similarity between two field stray distributions, curved hollow nanoshell with the uniform thickness produces a sharply localized stray field with a rapid decrease of the absolute value of the vector potential with the distance, see Figure 4c–e.

In the case of the curved nanoshell with asymmetric thickness distribution, uncompensated magnetostatic charges distributed along the hollow shell generate $\boldsymbol{A}$ with gradual decay extending far from the DW region, see Figure 4f–h. This gradual decay reflects the extended influence of the magnetostatic charges, resulting in a more spatially widespread stray field configuration compared to the hollow shell with a symmetric thickness profile, see Figure 4g,h. Thus, the asymmetry of the Co_3Fe shell thickness profile opens up the possibility of controlling the distribution of the scattered field caused by the structural imbalance of magnetostatic charges.

The possibility to tailor the spatial distribution of stray fields and vector potentials through geometrical features of core–shell heterostructures provides a powerful route to the functional design of hybrid electronic systems. In particular, localized vector-potential and stray-field profiles enable fabrication of hybrid 2D/3D superconductor/ferromagnet (S/F) architectures, with 3D curved hollow magnetic nanoshells fabricated above 2D superconducting nanostripes. In such configuration, stabilized VHV DWs would interact with superconducting vortices via tailored stray fields, creating vortex pinning potentials and imposing position-dependent phase biases in Josephson weak links. These configurations extend the functionality of planar S/F heterostructures, where DWs or patterned nanomagnets manipulate superconducting vortices [62–65], introduce pinning landscapes [66], control Josephson phases [67], or generate local Josephson vortices using

16163028, 2026, 50, Downloaded from https://advanced.onlinelibrary.wiley.com/doi/10.1002/adfm.202523172 by Helmholtz-Zentrum Berlin Für, Wiley Online Library on [20/07/2026]. See the Terms and Conditions (https://onlinelibrary.wiley.com/terms-and-conditions) on Wiley Online Library for rules of use; OA articles are governed by the applicable Creative Commons License

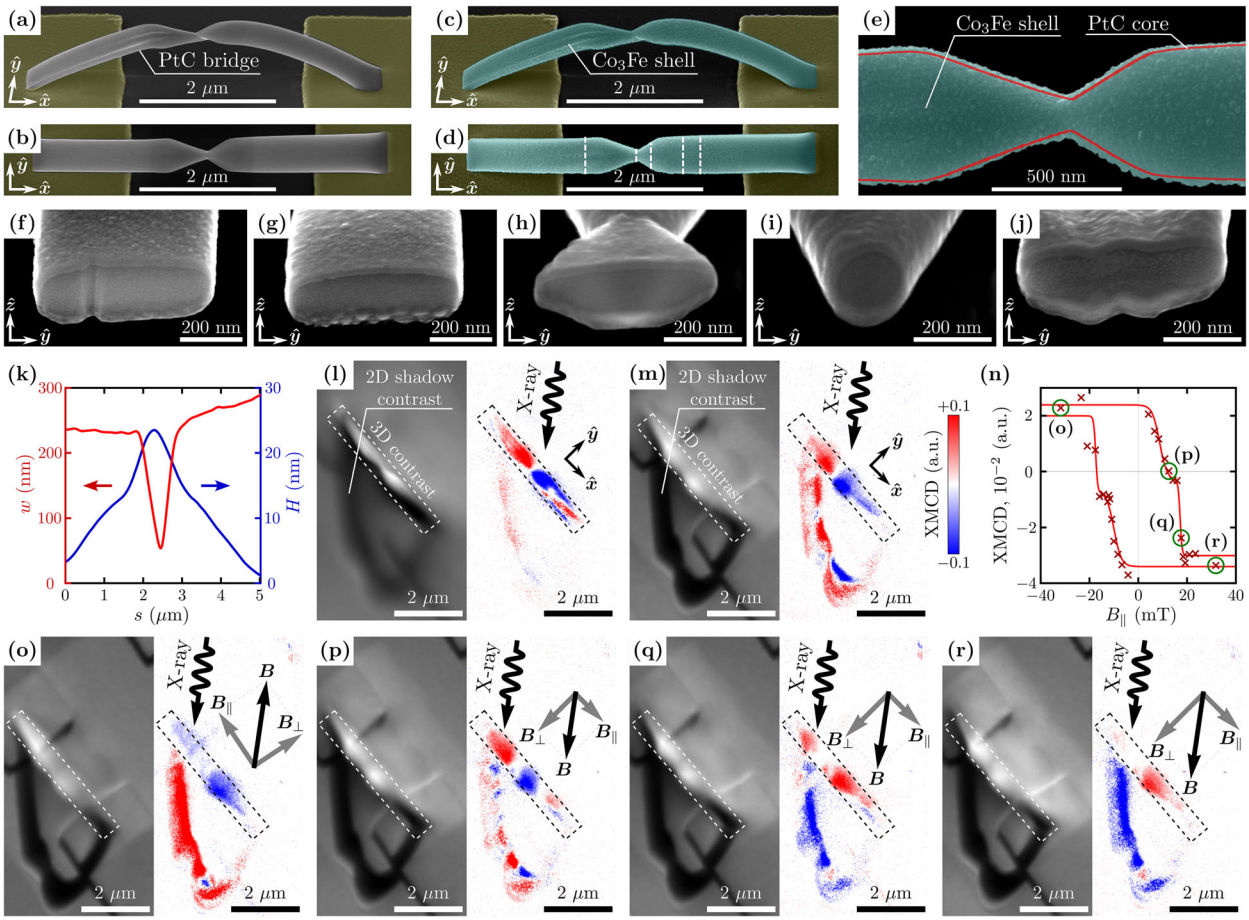

FIGURE 5 | Structural and magnetic characterization of a core–shell heterostructure with a constriction. (a,b) and (c,d) Artificially colored SEM images of the side and top views of the curved 3D PtC scaffold and resulting PtC/Co_3Fe core–shell heterostructure after site-selective CVD, respectively. Dashed lines indicate the positions of the focused ion beam slices depicted in (f–j). (e) High-resolution top-view SEM image of the constriction, with an overlaid contour of the initial PtC scaffold, which reveals local widening of the Co_3Fe shell. (f–j) Side-view SEM images of different cross-sections of the 3D heterostructure, which demonstrate the change in profile in the constriction areas. The sequence of FIB cuts is taken from the right side of the heterostructure depicted in (d). (k) Line profiles of the PtC core width, w, and Co_3Fe shell thickness, H, as a function of the arc length, s, along the curved 3D heterostructure with a constriction, respectively. (l) and (m) show XMCD-PEEM contrasts of the geometrically constricted PtC/Co_3Fe core–shell nanostructure with a focus on the top part of the bridge apex (direct contrast) and on the shadow (shadow contrast), respectively. (n) Hysteresis-type measurement of the experimentally obtained averaged shadow XMCD signal (red crosses). The red line shows the experimental data fitting. (o–r) Shadow XMCD-PEEM scans of the core–shell heterostructure with the constriction imaged at remanence after the application of the external magnetic fields $B = -47.5;\ 18.8;\ 26.3;\ 47.5$ mT (corresponding longitudinal field components $B_{\parallel} = -31.8;\ 12.5;\ 17.6;\ 31.8$ mT), respectively.

inhomogeneous fields from magnetic force microscopy tips [68, 69].

2.4 | Magnetic Nanoshells With Inhomogeneous First and Second Principal Curvatures

To investigate the impact of longitudinally inhomogeneous first, κ_1, and second, κ_2, principal curvatures on magnetic responses, we introduced a geometrical constriction in the middle of the PtC scaffold nanostructure during the FEBID process, see Figure 5a,b. This constriction is formed between two smoothly curved flattened segments and creates a necked region where the scaffold width narrows from ≈240 nm in the left curved part to ≈80 nm in the constriction and then widens again to ≈290 nm in the right curved part, see Figure 5k. The subsequent site-selective CVD process results in the formation of a conformal Co_3Fe shell around both curved flattened segments and the constriction region of the PtC scaffold, see Figure 5c,d. However, due to the reduced cross-section, the constriction region generates an intense localized Joule heating due to the higher current density, which leads to a significantly increased Co_3Fe thickness in this region, Figure 5e. Specifically, the average magnetic-layer thickness varies continuously from several nanometres at both ends to ≈24 nm at the constriction region, see Figure 5k. Post-imaging cross-sectional SEM analysis reveals a pronounced thickness gradient and structural variations at the constriction, together with significant surface roughness and the polycrystalline nature of the magnetic nanoshell, see Figure 5f–j.

XMCD-PEEM visualization of the core–shell heterostructure in the as-prepared state employs both direct and shadow imaging modes to capture magnetization distribution of the top surface and through-thickness magnetic information, respectively, see Figure 5l,m. Direct image contrast reveals the formation of characteristic red-white-blue contrast in the constriction, which

16163028, 2026, 50, Downloaded from https://advanced.onlinelibrary.wiley.com/doi/10.1002/adfm.202523172 by Helmholtz-Zentrum Berlin Für, Wiley Online Library on [20/07/2026]. See the Terms and Conditions (https://onlinelibrary.wiley.com/terms-and-conditions) on Wiley Online Library for rules of use; OA articles are governed by the applicable Creative Commons License

corresponds to the formation of two differently oriented magnetic domains with respect to the direction of the X-ray beam and separated by a DW pinned at the constriction, see Figure 5l. The corresponding 2D shadow image of the heterostructure (Figure 5m) unveils the presence of complex red-white-blue patterns, which appear not only in the constriction shadow projection but also along the entire length of the shadow. This complex shadow pattern indicates the presence of a multidomain state on the bottom part of the Co_3Fe shell in addition to uniform domains in the upper part.

To investigate the formation of such a state, we conduct the hysteresis-type measurements with the in-plane magnetic field applied at −48° with respect to the longitudinal direction of the core–shell heterostructure. The magnetic hollow shell is sequentially imaged at remanence ($B = 0$ mT) after applying a magnetic field in the range $B \in [-50; 50]$ mT with the corresponding longitudinal component $B_{\parallel} \in [-33.5; 33.5]$ mT. These measurements yield a two-step hysteresis loop constructed from the averaged shadow XMCD-signal, which reveals switching events at $B_{\parallel}^{1} = 9.4$ mT and $B_{\parallel}^{2} = 17.3$ mT (Figure 5n). Detailed analysis of the XMCD contrasts across the hysteresis cycle reveals the evolution of the magnetic configuration, starting from the fully saturated state featuring a homogeneous blue direct contrast and predominantly red shadow contrast, see Figure 5o. The appearance of a small blue area in the shadow contrast indicates a pinned magnetic texture localized near the geometrical constriction, which remains pinned through the field reversal. Upon reaching the first switching field, $B_{\parallel}^{1}$, the direct contrast exhibits a pronounced change (Figure 5p), which indicates the propagation of a DW and its pinning at the geometrical constriction. Moreover, the shadow contrast reveals the formation of a complex multidomain state in the bottom part of the bridge.

Further increase of the magnetic field to $B_{\parallel}^{2}$ initiates the reversal of the remaining unswitched segment of the heterostructure, which results in almost homogeneous red direct contrast and predominantly blue shadow XMCD contrat, see Figure 5q. Despite this near-complete reversal, localized pinning sites in both sections of the core–shell structure give rise to residual inhomogeneities in the magnetic distribution, that are manifested as small residual features in the shadow contrast. These subtle contrast variations indicate the presence of minor pinned magnetic textures that persist beyond the main switching event and require an additional field increase for complete depinning, see Figure 5r. Such localized pinning is correlated with enhanced surface roughness and potential variations in material parameters, which occur from the polycrystalline nature of the Co_3Fe Shell due to high local temperature gradients near the constriction region. The average size of the magnetic crystallites being around 20 nm is of the same range with a theoretically predicted domain wall width, $\delta = \pi\,\ell = 10$ nm for Co_3Fe [70]. Still, despite the presence of pronounced surface roughness and polycrystalline nature of the magnetic nanoshell, the overall switching behavior of the core–shell heterostructure remains highly reproducible, consistently exhibiting DW pinning at the constriction region. This reproducibility suggests that the dominant contributions to the pinning mechanism originates from the structural characteristics of the constriction itself, e.g. the longitudinal thickness gradients [21, 71] and cross-section variations [31] that give rise to strong curvature gradients [72]. The combined effect of which creates a robust potential landscape that stabilize DW at the constriction during the magnetization reversal. Still, the complex interplay of morphological, structural and material parameters makes a reliable qualitative analysis by micromagnetic simulations challenging, as such models would obtain significant assumptions regarding local roughness, thickness and magnetic parameters variations. Therefore, in this work, we limit our analysis to experimentally observed XMCD-PEEM contrast evolution, which provides direct insight into the magnetization reversal and DW pinning in the constricted hollow magnetic nanoshells.

3 | Conclusion

In summary, we have demonstrated the fabrication of self-standing 3D PtC/Co_3Fe core–shell heterostructures with tailored morphological and geometrical properties using a hybrid approach, which combines FEBID and site-selective CVD. The precise control over the curvilinear geometry of PtC scaffolds, combined with engineered thermal gradients during CVD for Co_3Fe shell preparation, allows the realization of versatile magnetic geometries and thickness distributions within the framework of one material system. The performed XMCD-PEEM investigation, combined with full-scale micromagnetic simulations, reveals the critical influence of geometry and shell morphology on the magnetization configuration and switching behavior in these nanostructures. Specifically, we show that a narrow hollow magnetic shell exhibits single-step magnetization reversal with the formation of a VHV DW, while wider ones with asymmetrical shell thickness support a two-step switching process mediated by the localized reversal of distinct regions. The introduction of a geometrical constriction at the magnetic nanoshell centre provides a robust pinning site for DWs and potential stabilization of multidomain states due to the pronounced surface roughness.

Furthermore, the versatility of the fabricated core–shell magnetic geometries not only enhance the complexity of micromagnetic textures, but also strongly influences the spatial configurations of the stray magnetic fields and tunes the vector potential "footprint" surrounding the hollow magnetic shell. The spatially distinct electromagnetic signature could offer valuable capabilities for the future quantum technologies by enabling localized control of superconducting vortex dynamics and phase shift manipulation inside the Josephson junction. Still, remaining challenges in achieving defect-free scalability and precise thickness control require further experimental studies. In particular, the influence of temperature gradients on the asymmetry of the magnetic nanoshell creates significant scope for micromagnetic studies of the interplay between scaffold geometry, layer thickness, and curvature, which paves the way for experimental verification of theoretically predicted non-local curvilinear effects in tubular structures [31].

4 | Methods

4.1 | Sample Preparation

The PtC/Co_3Fe core–shell heterostructures discussed in the main text are fabricated by means of FEBID inside a dual-beam SEM/FIB microscope (FEI, Nova NanoLab 600) equipped

16163028, 2026, 50, Downloaded from https://advanced.onlinelibrary.wiley.com/doi/10.1002/adfm.202523172 by Helmholtz-Zentrum Berlin Für, Wiley Online Library on [20/07/2026]. See the Terms and Conditions (https://onlinelibrary.wiley.com/terms-and-conditions) on Wiley Online Library for rules of use; OA articles are governed by the applicable Creative Commons License

with a Schottky electron emitter. Two different precursor gases $(CH_3)_3CH_3C_5H_4Pt$ and $HFeCo_3(CO)_{12}$ are supplied through gas injection systems (GIS) having the same 50° inclination relative to the substrate, but located at opposite sides of the SEM chamber. During the FEBID process, electron-beam-induced dissociation of $(CH_3)_3CH_3C_5H_4Pt$ forms a carbon-rich PtC scaffold, while the remaining carbon leftovers are removed from the chamber. The precursor gas is supplied via a GIS with a capillary of 0.5 mm inner diameter being positioned 100 μm above the growth area. The base pressure of the SEM chamber is 5×10^{-7} mbar, which increases to 1×10^{-5} mbar during the FEBID process. The electron beam parameters are 30 kV for the acceleration voltage and 15 pA for the beam current.

The fabrication of various 3D geometries using FEBID is enabled by a versatile pattern-generation approach [35, 73]. In the present work, the PtC nanostructures are grown using a heuristic approach: the scaffold shape is obtained by varying the beam dwell time at specific locations, t_D, between 300 μs and 20 ms using an exponential function. The growth starts after tilting the stage to $\approx 52°$, while the electron beam falls vertically downward and moves between two Cr (10 nm)/Au (50 nm) contacts prepared by means of optical lithography on SiO_2 (200 nm)/Si wafer. Local morphological features, such as wire bending or geometric constrictions, are created by controlling the direction and speed of the electron beam during FEBID growth.

After the fabrication, the PtC scaffold is irradiated again by the electron beam in the absence of a precursor gas to reduce its porosity and improve conductivity. This step is essential for the subsequent site-selective CVD process, during which a dc bias current is applied to the PtC bridge in the atmosphere of the $HFeCo_3(CO)_{12}$ gas. The latter is introduced to the SEM by means of the second GIS positioned at 100 μm above the growth area and tilted at 50° to the substrate surface. During the CVD process, a conformal Co_3Fe magnetic shell is formed around the PtC scaffold due to the $HFeCo_3(CO)_{12}$ precursor thermal decomposition by means of Joule heating. In particular, to produce the narrow core–shell nanostructure without a constriction, a constant dc current of 25 μA was applied for 71 s; for the wide nanostructure, 20 μA was applied for 125 s, followed by 100 μA for 42 s. For the PtC/Co_3Fe core–shell nanostructure with a constriction, the dc current was 30 μA for the first deposition cycle and 70 μA for the second. The growth rate of a magnetic core–shell layer is monitored through the in situ resistance change of the bridge, as the deposited Co_3Fe layer reduces the total resistance across the entire heterostructure. The growth process continues until the temperature drops to below the cut-off temperature (423 K) for thermally-induced dissociation of the $HFeCo_3(CO)_{12}$ gas [39].

4.2 | XMCD-PEEM Measurements

The FEBID-grown core–shell nanobridges are investigated by means of X-ray magnetic circular dichroism photoelectron emission microscopy (XMCD-PEEM) [55]. Measurements are carried out at BESSY II synchrotron (SPEEM beamline UE49-PGM, Helmholtz–Zentrum Berlin, Germany) with a circularly polarized X-ray beam at the L_3 edge of Co. Experiments are conducted at 10 keV extraction voltage to minimize the risk of electrical discharges from 3D nanostructures, compared to standard 20 keV. This voltage reduction degrades spatial resolution by a factor of 1.4 (to approximately 60 nm), which is partially compensated by the better energy filtering and hence lower chromatic aberration. XMCD imaging is performed in two different modes: (i) with the focus on the top bridge surface to visualize the magnetization state on it, and (ii) on its shadow, which allows to extract information from the entire sample. While the first method is more suitable for visualizing non-trivial magnetization distributions in planar samples, the second one is utilized for the imaging of 3D magnetic geometries [54, 74]. The latter benefits from the incident angle of the X-ray beam, which falls at a shallow angle of 16° to the sample surface and enhances the spatial resolution along the projection direction [55, 56]. The magnetic imaging is performed at non-zero azimuthal angles between the beam direction and bridge axes to enable better visualization of equilibrium states, as the XMCD-PEEM technique is insensitive to magnetization vectors directed perpendicular to the beam direction. Namely, the XMCD contrast detects only magnetization components being parallel or antiparallel to the beam. The magnetic samples are installed in a sample holder with a built-in electromagnet, which creates the in-plane magnetic field in the range $B = [-50; +50]$ mT aligned along the X-ray azimuthal direction. For each type of 3D core–shell heterostructure, we performed multiple hysteresis-like XMCD-PEEM measurements, in which the sample was saturated and then subjected to an in-plane field of opposite polarity, followed by remanent imaging. In total, we recorded on the order of 5 – 10 complete cycles per structure and in all cases the observed contrasts were reproducible from cycle to cycle. For the curved core–shell heterostructures without a constriction, hysteresis-like signals were obtained from the averaged direct XMCD-PEEM contrast and fitted with a single hyperbolic tangent function, whereas for the constricted heterostructure the hysteresis loop was obtained from the averaged shadow contrast (resulting in an inverted loop) and fitted with the sum of two hyperbolic tangent functions to reproduce the two-step switching behavior.

4.3 | Micromagnetic Simulations

The full-scale micromagnetic simulations are performed for experimentally-obtained 3D core–shell bridge geometries using the GPU-accelerated *tetmag* software based on the finite element method (FEM) [75]. The experimental geometries are reconstructed from high-resolution SEM images obtained during the fabrication procedure, and then they are converted into a 3D tetrahedron mesh with an average size of 6 nm. Computations are done for the micromagnetic parameters of Co_3Fe polycrystalline media: saturation magnetization $\mu_0 M_s = 1.88$ T, where μ_0 is the vacuum permeability, exchange constant $A = 14$ pJ/m, which corresponds to the exchange length $\ell = \sqrt{2A/(\mu_0 M_s^2)} = 3.2$ nm. To calculate the hysteresis loops for each core–shell nanobridge, we apply a magnetic field at the angle $\alpha_B = 32°$ to the long axis of the bridge, starting from positive $B_{max} = +100$ mT to $B_{min} = -100$ mT with a field step of $\Delta B = -1$ mT. After each change of the external field, the magnetic system is allowed to converge to equilibrium through the minimization of the local torque exerted by the effective field $\boldsymbol{H}_{eff}$ on the normalized magnetization $\boldsymbol{m} = \boldsymbol{M}/M_s$. To determine the equilibrium magnetic states, we conduct additional micromagnetic simulations using pre-determined states: homogeneously magnetized along $\hat{\boldsymbol{x}}$, $\hat{\boldsymbol{y}}$

16163028, 2026, 50, Downloaded from https://advanced.onlinelibrary.wiley.com/doi/10.1002/adfm.202523172 by Helmholtz-Zentrum Berlin Für, Wiley Online Library on [20/07/2026]. See the Terms and Conditions (https://onlinelibrary.wiley.com/terms-and-conditions) on Wiley Online Library for rules of use; OA articles are governed by the applicable Creative Commons License

and $\hat{\boldsymbol{z}}$ directions, random ones, and artificially determined DWs with various symmetries and positions. The calculations are performed for experimentally defined, straight, and ideal tubular shell geometries with various shapes.

4.4 | XMCD-PEEM Reconstruction

To interpret the experimentally-obtained direct and shadow XMCD-PEEM contrasts for curved core–shell heterostructures (PtC core/Co_3Fe shell), we developed a ray-tracing simulation that calculates progressive X-ray absorption along each ray path for the micromagnetically obtained states. Following the quantitative analysis described in ref. [56], the simulation accounts the intersection of each structural element of the simulated 3D core–shell structure with the X-ray beam and the corresponding attenuation in each layer, including helicity-dependent absorption in the Co_3Fe shell. The simulations are performed at an experimental incidence angle of 16° and an azimuthal angle of 32°, see Figure S4a. To prevent moiré pattern formation in direct and shadow contrasts, X-ray beams are distributed randomly within a smooth kernel density distribution of projected points from the 3D mesh geometry, Figure S4b. The corresponding progressive X-ray absorption along each ray path element, dl, inside the Co_3Fe nanoshell is calculated as follows:

$$\frac{dI_X^{\pm}(l)}{dl} = -I_X^{\pm}(l)\left\{\left[\frac{\mu_{Co}^{+}}{2}(1 \pm \boldsymbol{m}(l)\cdot\boldsymbol{k}) + \frac{\mu_{Co}^{-}}{2}(1 \mp \boldsymbol{m}(l)\cdot\boldsymbol{k})\right] \times c_{Co} + \mu_{Fe}(1 - c_{Co})\right\} \quad (1)$$

while inside the PtC core it is following:

$$\frac{dI_X^{\pm}(l)}{dl} = -I_X^{\pm}(l)\left\{c_{Pt}\,\mu_{Pt} + (1 - c_{Pt})\mu_C\right\} \quad (2)$$

where $c_{Co} = 75\%$ and $c_{Pt} = 30\%$ are volume concentrations of Co in the Co_3Fe shell and Pt in the PtC core, respectively, derived from Ref. [39]. The corresponding linear absorption coefficients for the Co L3 edge (777 eV) are derived from [76, 77]: $\mu_{Co}^{+} = 8\times10^{-2}$ nm^{-1}, $\mu_{Co}^{-} = 4.7\times10^{-2}$ nm^{-1}, $\mu_{Fe} = 12.5\times10^{-3}$ nm^{-1}, $\mu_{Pt} = 13\times10^{-3}$ nm^{-1} and $\mu_C = 8\times10^{-4}$ nm^{-1}. In Equation (1), $\boldsymbol{k}$ is the propagation vector of the X-ray beam and $\boldsymbol{m}(\boldsymbol{r})$ is the local magnetization distribution. Integrating the progressive absorption Equations (1) and (2) along each ray path yields transmitted beam intensities for both polarizations (I_X^{+} and I_X^{-}), from which the shadow XMCD contrast is obtained:

$$\eta_X = \frac{I_X^{+} - I_X^{-}}{I_X^{+} + I_X^{-}} \quad (3)$$

The resulting simulated XMCD-PEEM shadow contrast η_{XMCD} is represented using blue-white-red colors, which correspond to magnetization components being parallel, perpendicular and antiparallel to the X-ray beam, respectively [55].

To simulate the direct XMCD contrast, we calculate local photoelectron emission rates for both polarizations, $I_E^{\pm}$, from each point of the magnetic surface, see Figure S4d. In this case, the number of secondary photoelectrons created at depth, dt, is calculated based on the local absorption of the transmitted X-ray intensity [77]:

$$dI_{E,0}^{\pm} = \frac{dI_X^{\pm}}{dt}dt \quad (4)$$

However, it should be taken into account that not all created electrons can reach the surface of the sample, which leads to their effective reduction in accordance with the electron escape depth, $\lambda_e = 2.5$ nm [77]. Thus, the resulting photoelectron yield in the direction of the detector from the surface is

$$dI_E^{\pm} = dI_{E,0}^{\pm}\, exp\left[-\frac{t}{\lambda_e}\right] \quad (5)$$

To reconstruct the 3D direct and 3D shadow XMCD contrasts from the top surface of core–shell heterostructure, we project a regular rectangular 2D grid onto the XY-plane mimicking detector pixels. For each grid cell, the total photoelectron emission, $I_{E,\Sigma}^{\pm}$, integrates contributions from all depths along each X-ray beam, that intersects the chosen cell within the Co_3Fe shell. The final direct XMCD contrast is then computed as

$$\eta_E = \frac{I_E^{+} - I_E^{-}}{I_E^{+} + I_E^{-}} \quad (6)$$

which can be directly compared with experimentally obtained direct contrasts.

4.5 | Stray Field Calculation

To investigate the stray field distributions around the 3D curved hollow magnetic shells, we conduct additional numerical calculations for equilibrium magnetization distributions obtained for experimental geometries with both types of symmetric and asymmetric thickness distributions. The method is based on numerical calculation of the coordinate distribution of the vector potential, $\boldsymbol{A}(\boldsymbol{r})$, and the corresponding calculation of the stray field $\boldsymbol{H}(\boldsymbol{r}) = [\nabla\times\boldsymbol{A}(\boldsymbol{r})]/\mu_0$ (with $\boldsymbol{B}(\boldsymbol{r}) = \nabla\times\boldsymbol{A}(\boldsymbol{r})$) outside the magnet in the surrounding volume, V, around the magnetic geometry with additional spacing ("airbox") [78]:

$$\nabla^2\boldsymbol{A}(\boldsymbol{r}) = \begin{cases} -\mu_0\boldsymbol{J}(\boldsymbol{r}) & \text{inside the magnetic volume} \\ 0 & \text{outside the magnetic volume} \end{cases} \quad (7)$$

where the Coulomb gauge is used. This calculation utilizes the Ampère approach and replaces the magnetization by an equivalent distribution of the current density, $\boldsymbol{J}(\boldsymbol{r}) = \nabla\times\boldsymbol{M}(\boldsymbol{r})$. The Equation (7) is solved numerically with the corresponding boundary conditions at the airbox volume surface S:

$$A_x(\boldsymbol{r})\Big|_S = 0, \quad A_y(\boldsymbol{r})\Big|_S = 0, \quad A_z(\boldsymbol{r})\Big|_S = 0 \quad (8)$$

It should be noted that the imposed boundary conditions force magnetic flux lines to intersect the airbox boundary perpendicularly, which may affect the appearance of the field distribution near its outer surface. In particular, this boundary effect can distort the flux-line visualization at larger distances from the core–shell geometry, while the near-field distribution around the core–shell magnetic nanostructures remains reliable.

16163028, 2026, 50, Downloaded from https://advanced.onlinelibrary.wiley.com/doi/10.1002/adfm.202523172 by Helmholtz-Zentrum Berlin Für, Wiley Online Library on [20/07/2026]. See the Terms and Conditions (https://onlinelibrary.wiley.com/terms-and-conditions) on Wiley Online Library for rules of use; OA articles are governed by the applicable Creative Commons License

Acknowledgments

We thank Dr. Oleksandr V. Pylypovskyi and Dr. Attila Kakay (HZDR) for fruitful discussions. This work has been supported in part via German Research Foundation (Grants No. MA5144/24-1, MA5144/33-1, MA5144/39-1, No. HU752/16-1, No. HU752/19-1, No. VO2598/1-1, No. BA6595/5-1 and No. BA6595/2-2) under CRC/TRR 288 (Project No. A04) and ERC grant 3DmultiFerro (Project No. 101141331). Numerical calculations have been performed using the Hemera high-performance cluster at the HZDR [79].

Conflicts of Interest

The authors declare no conflicts of interest.

Data Availability Statement

The data that support the findings of this study are available from the corresponding author upon reasonable request.

References

1. D. Makarov, O. M. Volkov, A. Kákay, O. V. Pylypovskyi, B. Budinská, and O. V. Dobrovolskiy, "New Dimension in Magnetism and Superconductivity: 3D and Curvilinear Nano-Architectures," *Advanced Materials* 34 (2022): 2101758.

2. P. Gentile, M. Cuoco, O. M. Volkov, et al., "Electronic Materials with Nanoscale Curved Geometries," *Nature Electronics* 5 (2022): 551.

3. R. Winkler, F.-P. Schmidt, U. Haselmann, et al., "Direct-Write 3D Nanoprinting of Plasmonic Structures," *ACS Applied Materials and Interfaces* 9 (2017): 8233.

4. Y. Gaididei, V. P. Kravchuk, and D. D. Sheka, "Curvature Effects in Thin Magnetic Shells," *Physical Review Letters* 112 (2014): 257203.

5. O. M. Volkov, A. Kákay, F. Kronast, et al., "Experimental Observation of Exchange-Driven Chiral Effects in Curvilinear Magnetism," *Physical Review Letters* 123 (2019): 077201.

6. O. M. Volkov, D. Wolf, O. V. Pylypovskyi, et al., "Chirality Coupling in Topological Magnetic Textures with Multiple Magnetochiral Parameters," *Nature Communications* 14 (2023): 1491.

7. O. Bezsmertna, R. Xu, O. Pylypovskyi, et al., "Magnetic Solitons in Hierarchical 3D Magnetic Nanoarchitectures of Nanoflower Shape," *Nano Letters* 24 (2024): 15774.

8. V. P. Kravchuk, U. K. Rößler, O. M. Volkov, et al., "Topologically Stable Magnetization States on a Spherical Shell: Curvature-Stabilized Skyrmions," *Physical Review B* 94 (2016): 144402.

9. V. P. Kravchuk, D. D. Sheka, A. Kákay, et al., "Multiplet of Skyrmion States on a Curvilinear Defect: Reconfigurable Skyrmion Lattices," *Physical Review Letters* 120 (2018): 067201.

10. D. A. Dugato, W. B. F. Jalil, R. Cardias, et al., "Curved Nanomagnets: An Archetype for the Skyrmionic States at Ambient Conditions," *Nano Letters* 25 (2025): 8901.

11. O. M. Volkov, O. V. Pylypovskyi, F. Porrati, et al., "Three-Dimensional Magnetic Nanotextures with High-Order Vorticity in Soft Magnetic Wireframes," *Nature Communications* 15 (2024): 2193.

12. G. Williams, M. Hunt, B. Boehm, et al., "Two-Photon Lithography for 3D Magnetic Nanostructure Fabrication," *Nano Research* 11 (2018): 845.

13. M. Hunt, M. Taverne, J. Askey, et al., "Harnessing Multi-Photon Absorption to Produce Three-Dimensional Magnetic Structures at the Nanoscale," *Materials* 13 (2020): 761.

14. J. Askey, M. O. Hunt, L. Payne, et al., "Direct Visualization of Domain Wall Pinning in Sub-100 nm 3D Magnetic Nanowires with Cross-Sectional Curvature," *Nanoscale* 16 (2024): 17793.

15. A. M. A. Farinha, S.-H. Yang, J. Yoon, B. Pal, and S. S. P. Parkin, "Interplay of Geometrical and Spin Chiralities in 3D Twisted Magnetic Ribbons," *Nature* 639 (2025): 67.

16. W. Jung, Y.-H. Jung, P. V. Pikhitsa, et al., "Three-Dimensional Nanoprinting via Charged Aerosol Jets," *Nature* 592 (2021): 54.

17. J. M. D. Teresa, A. Fernández-Pacheco, R. Córdoba, L. Serrano-Ramón, S. Sangiao, and M. R. Ibarra, "Review of Magnetic Nanostructures Grown by Focused Electron Beam Induced Deposition (FEBID)," *Journal of Physics D: Applied Physics* 49 (2016): 243003.

18. M. Huth, F. Porrati, and O. Dobrovolskiy, "Focused Electron Beam Induced Deposition Meets Materials Science," *Microelectronic Engineering* 185–186 (2018): 9.

19. L. Skoric, D. Sanz-Hernández, F. Meng, C. Donnelly, S. Merino-Aceituno, and A. Fernández-Pacheco, "Layer-by-Layer Growth of Complex-Shaped Three-Dimensional Nanostructures with Focused Electron Beams," *Nano Letters* 20 (2020): 184.

20. D. Sanz-Hernández, A. Hierro-Rodriguez, C. Donnelly, et al., "Artificial Double-Helix for Geometrical Control of Magnetic Chirality," *ACS Nano* 14 (2020): 8084.

21. M.-A. Mawass, K. Richter, A. Bisig, et al., "Switching by Domain-Wall Automotion in Asymmetric Ferromagnetic Rings," *Physical Review Applied* 7 (2017): 044009.

22. E. Berganza, F. Tejo, G. H. R. Bittencourt, V. L. Carvalho-Santos, O. Chubykalo-Fesenko, and A. Asenjo, "Experimental Evidence of Curvature Gradient Driven Domain Wall Automotion," *Small* 21 (2025): 2407084.

23. M. A. Mamoori, L. Keller, J. Pieper, et al., "Magnetic Characterization of Direct-Write Free-Form Building Blocks for Artificial Magnetic 3D Lattices," *Materials* 11 (2018): 289.

24. L. Keller and M. Huth, "Pattern Generation for Direct-Write Three-Dimensional Nanoscale Structures via Focused Electron Beam Induced Deposition," *Beilstein Journal of Nanotechnology* 9 (2018): 2581.

25. N. P. Jochmann, A. Salvador-Porroche, and S. Barth, "Beyond the Beam: Exploring Charged Particle Nanoprinting," *Advanced Functional Materials* 35 (2025): e07465, https://doi.org/10.1002/adfm.202507465.

26. C. Donnelly, A. Hierro-Rodríguez, C. Abert, et al., "Complex Free-Space Magnetic Field Textures Induced by Three-Dimensional Magnetic Nanostructures," *Nature Nanotechnology* 17 (2022): 136.

27. J. Fullerton, A. R. C. McCray, A. K. Petford-Long, and C. Phatak, "Understanding the Effect of Curvature on the Magnetization Reversal of Three-Dimensional Nanohelices," *Nano Letters* 24 (2024): 2481.

28. F. Meng, C. Donnelly, C. Abert, et al., "Non-Planar Geometrical Effects on the Magnetoelectrical Signal in a Three-Dimensional Nanomagnetic Circuit," *ACS Nano* 15 (2021): 6765.

29. J. A. Otálora, M. Yan, H. Schultheiss, R. Hertel, and A. Kákay, "Curvature-Induced Asymmetric Spin-Wave Dispersion," *Physical Review Letters* 117 (2016): 227203.

30. J. A. Otálora, M. Yan, H. Schultheiss, R. Hertel, and A. Kákay, "Asymmetric Spin-Wave Dispersion in Ferromagnetic Nanotubes Induced by Surface Curvature," *Physical Review B* 95 (2017): 184415.

31. D. D. Sheka, O. V. Pylypovskyi, P. Landeros, Y. Gaididei, A. Kákay, and D. Makarov, "Nonlocal Chiral Symmetry Breaking in Curvilinear Magnetic Shells," *Communications Physics* 3 (2020): 128.

32. P. Landeros and A. S. Núñez, "Domain Wall Motion on Magnetic Nanotubes," *Journal of Applied Physics* 108 (2010): 033917.

33. M. Yan, C. Andreas, A. Kákay, F. García-Sánchez, and R. Hertel, "Fast Domain Wall Dynamics in Magnetic Nanotubes: Suppression of Walker Breakdown and Cherenkov-Like Spin Wave Emission," *Applied Physics Letters* 99 (2011): 122505.

34. R. Hertel, "Ultrafast Domain Wall Dynamics in Magnetic Nanotubes and Nanowires," *Journal of Physics: Condensed Matter* 28 (2016): 483002.

16163028, 2026, 50, Downloaded from https://advanced.onlinelibrary.wiley.com/doi/10.1002/adfm.202523172 by Helmholtz-Zentrum Berlin Für, Wiley Online Library on [20/07/2026]. See the Terms and Conditions (https://onlinelibrary.wiley.com/terms-and-conditions) on Wiley Online Library for rules of use; OA articles are governed by the applicable Creative Commons License

35. L. Keller, M. K. I. A. Mamoori, J. Pieper, et al., "Direct-Write of Free-Form Building Blocks for Artificial Magnetic 3D Lattices," *Scientific Reports* 8 (2018): 6160.

36. A. Weitzer, M. Huth, G. Kothleitner, and H. Plank, "Expanding FEBID-Based 3D-Nanoprinting Toward Closed High-Fidelity Nanoarchitectures," *ACS Applied Electronic Materials* 4 (2022): 744.

37. A. Kuprava and M. Huth, "Precursor Sticking Coefficient Determination from Indented Deposits Fabricated by Electron Beam Induced Deposition," *Beilstein Journal of Nanotechnology* 16 (2025): 35.

38. C. Fernández-González, P. Morales-Fernández, L. A. Turnbull, et al., "Realization of Complex-Shaped Magnetic Nanotubes with 3D Printing and Electrodeposition," *Advanced Functional Materials* 36 (2025): e15722.

39. F. Porrati, S. Barth, G. C. Gazzadi, et al., "Site-Selective Chemical Vapor Deposition on Direct-Write 3D Nanoarchitectures," *ACS Nano* 17 (2023): 4704.

40. F. Porrati, M. Pohlit, J. Müller, et al., "Direct Writing of CoFe Alloy Nanostructures by Focused Electron Beam Induced Deposition from a Heteronuclear Precursor," *Nanotechnology* 26 (2015): 475701.

41. P. Landeros, S. Allende, J. Escrig, E. Salcedo, D. Altbir, and E. E. Vogel, "Reversal Modes in Magnetic Nanotubes," *Applied Physics Letters* 90 (2007): 102501.

42. P. Landeros, O. J. Suarez, A. Cuchillo, and P. Vargas, "Equilibrium States and Vortex Domain Wall Nucleation in Ferromagnetic Nanotubes," *Physical Review B* 79 (2009): 024404.

43. M. Yan, C. Andreas, A. Kákay, F. Garcia-Sanchez, and R. Hertel, "Chiral Symmetry Breaking and Pair-Creation Mediated Walker Breakdown in Magnetic Nanotubes," *Applied Physics Letters* 100 (2012): 252401.

44. J. Otálora, J. López-López, P. Vargas, and P. Landeros, "Chirality Switching and Propagation Control of a Vortex Domain Wall in Ferromagnetic Nanotubes," *Applied Physics Letters* 100 (2012): 072407.

45. M. Staňo, S. Schaefer, A. Wartelle, et al., "Flux-Closure Domains in High Aspect Ratio Electroless-Deposited CoNiB Nanotubes," *SciPost Physics* 5 (2018): 038.

46. L. Skoric, C. Donnelly, C. Abert, A. Hierro-Rodriguez, D. Suess, and A. Fernández-Pacheco, "Micromagnetic Modeling of Magnetic Domain Walls in Curved Cylindrical Nanotubes and Nanowires," *Applied Physics Letters* 118 (2021): 242403.

47. L. Körber, R. Verba, J. A. Otálora, et al., "Curvilinear Spin-Wave Dynamics Beyond the Thin-Shell Approximation: Magnetic Nanotubes as a Case Study," *Physical Review B* 106 (2022): 014405.

48. E. Saavedra, S. Castillo-Sepúlveda, R. Corona, D. Altbir, J. Escrig, and V. Carvalho-Santos, "Influence of Curvature on the Dynamical Susceptibility of Bent Nanotubes," *Results in Physics* 35 (2022): 105290.

49. M. Wyss, A. Mehlin, B. Gross, et al., "Imaging Magnetic Vortex Configurations in Ferromagnetic Nanotubes," *Physical Review B* 96 (2017): 024423.

50. M. Zimmermann, T. N. G. Meier, F. Dirnberger, et al., "Origin and Manipulation of Stable Vortex Ground States in Permalloy Nanotubes," *Nano Letters* 18 (2018): 2828.

51. L. Körber, G. Quasebarth, A. Otto, and A. Kákay, "Finite-Element Dynamic-Matrix Approach for Spin-Wave Dispersions in Magnonic Waveguides with Arbitrary Cross Section," *AIP Advances* 11 (2021): 095006.

52. M. Staňo and O. Fruchart, "Magnetic Nanowires and Nanotubes," in *Handbook of Magnetic Materials* (Elsevier, 2018), 155–267.

53. F. Porrati, R. Sachser, C. H. Schwalb, A. S. Frangakis, and M. Huth, "Tuning the Electrical Conductivity of Pt-Containing Granular Metals by Postgrowth Electron Irradiation," *Journal of Applied Physics* 109 (2011): 063715, https://doi.org/10.1063/1.3559773.

54. J. Kimling, F. Kronast, S. Martens, et al., "Photoemission Electron Microscopy of Three-Dimensional Magnetization Configurations in Core-Shell Nanostructures," *Physical Review B* 84 (2011): 174406.

55. R. Streubel, V. P. Kravchuk, D. D. Sheka, et al., "Equilibrium Magnetic States in Individual Hemispherical Permalloy Caps," *Applied Physics Letters* 101 (2012): 132419.

56. S. Jamet, S. D. Col, N. Rougemaille, et al., "Quantitative Analysis of Shadow X-Ray Magnetic Circular Dichroism Photoemission Electron Microscopy," *Physical Review B* 92 (2015): 144428, https://doi.org/10.1103/physrevb.92.144428.

57. J. Yang, J. Kim, B. Kim, Y.-J. Cho, J.-H. Lee, and S.-K. Kim, "Vortex-Chirality-Dependent Standing Spin-Wave Modes in Soft Magnetic Nanotubes," *Journal of Applied Physics* 123 (2018): 033901.

58. R. Wieser, U. Nowak, and K. D. Usadel, "Domain Wall Mobility in Nanowires: Transverse Versus Vortex Walls," *Physical Review B* 69 (2004): 064401.

59. S. Ruiz-Gómez, C. Abert, P. Morales-Fernández, et al., "Tailoring the Energy Landscape of a Bloch Point Domain Wall with Curvature," *Nature Communications* 16 (2025): 7422.

60. K. V. Yershov, V. P. Kravchuk, D. D. Sheka, and Y. Gaididei, "Curvature-Induced Domain Wall Pinning," *Physical Review B* 92 (2015): 104412.

61. K. V. Yershov, V. P. Kravchuk, D. D. Sheka, O. V. Pylypovskyi, D. Makarov, and Y. Gaididei, "Geometry-Induced Motion of Magnetic Domain Walls in Curved Nanostripes," *Physical Review B* 98 (2018): 060409.

62. A. Y. Aladyshkin, A. V. Silhanek, W. Gillijns, and V. V. Moshchalkov, "Nucleation of Superconductivity and Vortex Matter in Superconductor–Ferromagnet Hybrids," *Superconductor Science and Technology* 22 (2009): 053001.

63. P. E. Goa, H. Hauglin, Å. A. F. Olsen, D. Shantsev, and T. H. Johansen, "Manipulation of Vortices by Magnetic Domain Walls," *Applied Physics Letters* 82 (2003): 79.

64. J. I. Vestgården, D. V. Shantsev, Å. A. F. Olsen, et al., "Interaction Between Superconducting Vortices and a Bloch Wall in Ferrite Garnet Films," *Physical Review Letters* 98 (2007): 117002.

65. V. Vlasko-Vlasov, U. Welp, G. Karapetrov, et al., "Guiding Superconducting Vortices with Magnetic Domain Walls," *Physical Review B* 77 (2008): 134518.

66. M. Iavarone, A. Scarfato, F. Bobba, et al., "Imaging the Spontaneous Formation of Vortex-Antivortex Pairs in Planar Superconductor/Ferromagnet Hybrid Structures," *Physical Review B* 84 (2011): 024506.

67. B. Baek, W. H. Rippard, S. P. Benz, S. E. Russek, and P. D. Dresselhaus, "Hybrid Superconducting-Magnetic Memory Device Using Competing Order Parameters," *Nature Communications* 5 (2014): 3888, https://doi.org/10.1038/ncomms4888.

68. V. V. Dremov, S. Y. Grebenchuk, A. G. Shishkin, et al., "Local Josephson Vortex Generation and Manipulation with a Magnetic Force Microscope," *Nature Communications* 10 (2019): 4009, https://doi.org/10.1038/s41467-019-11924-0.

69. G. Kim, J. Yun, J. Yang, et al., "Vortex Confinement Through an Unquantized Magnetic Flux," *NPG Asia Materials* 16 (2024): 44, https://doi.org/10.1038/s41427-024-00564-6.

70. A. Hubert and R. Schäfer, *Magnetic Domains: The Analysis of Magnetic Microstructures* (Springer Berlin Heidelberg, Berlin, 2009).

71. K. V. Yershov and D. D. Sheka, "Control of Magnetic Response in Curved Stripes by Tailoring the Cross Section," *Physical Review B* 107 (2023): L100415.

72. O. Pylypovskyi, D. Makarov, V. Kravchuk, A. Saxena, and D. Sheka, "Chiral Skyrmion and Skyrmionium States Engineered by the Gradient of Curvature", *Physical Review Applied* 10, (2018): 064057, https://doi.org/10.1103/PhysRevApplied.10.064057.

73. J. D. Fowlkes, R. Winkler, B. B. Lewis, et al., "High-Fidelity 3D-Nanoprinting via Focused Electron Beams: Computer-Aided Design (3BID)," *ACS Applied Nano Materials* 1 (2018): 1028.

16163028, 2026, 50, Downloaded from https://advanced.onlinelibrary.wiley.com/doi/10.1002/adfm.202523172 by Helmholtz-Zentrum Berlin Für, Wiley Online Library on [20/07/2026]. See the Terms and Conditions (https://onlinelibrary.wiley.com/terms-and-conditions) on Wiley Online Library for rules of use; OA articles are governed by the applicable Creative Commons License

74. S. Da Col, S. Jamet, N. Rougemaille, et al., "Observation of Bloch-Point Domain Walls in Cylindrical Magnetic Nanowires," *Physical Review B* 89 (2014): 180405.

75. R. Hertel, *tetmag, GitHub repository* (2023), https://github.com/R-Hertel/tetmag.

76. S. Seltzer, "Tables of X-Ray Mass Attenuation Coefficients and Mass Energy-Absorption Coefficients, NIST Standard Reference Database 126,".

77. R. Nakajima, J. Stöhr, and Y. U. Idzerda, "Electron-Yield Saturation Effects in L-Edge X-Ray Magnetic Circular Dichroism Spectra of Fe, Co, and Ni," *Physical Review B* 59 (1999): 6421.

78. J. Coey, *Magnetism and Magnetic Materials* (Cambridge University Press, 2009).

79. *High Performance Computing at Helmholtz-Zentrum Dresden-Rossendorf e.V.*, http://www.hzdr.de.

Supporting Information

Additional supporting information can be found online in the Supporting Information section.

Supporting File: adfm76069-sup-0001-SuppMat.pdf.

16163028, 2026, 50, Downloaded from https://advanced.onlinelibrary.wiley.com/doi/10.1002/adfm.202523172 by Helmholtz-Zentrum Berlin Für, Wiley Online Library on [20/07/2026]. See the Terms and Conditions (https://onlinelibrary.wiley.com/terms-and-conditions) on Wiley Online Library for rules of use; OA articles are governed by the applicable Creative Commons License